Enhanced porphyrin-based fluorescence imaging-guided photodynamic/photothermal synergistic cancer therapy by mitochondrial targeting

Denghui Shang[1,2†], Qilin Yu[3†], Wei Liu[2], Shouting Zhang[2], Yi Li[2], Jing Chen[1], Zhen Zhang[2*] and Xiaoquan Lu[1*]

ABSTRACT Mitochondria are the power plants of the cell and play key roles in activating the apoptotic pathway in cancer cells, which are readily susceptible to cytotoxic reactive oxygen species and temperature elevations. Herein, we develop a "nanomissile" that targets mitochondria to enhance tumor treatment effects by facilitating mitochondrial dysfunction and releasing cytochrome C to activate the apoptotic pathway of cancer cells under 650-nm laser irradiation. Porphyrin-grafted polydopamine nanomaterial (PTPF-MitP) is designed as a nanomissile, with integrated O_2-evolving photodynamic therapy and moderate photothermal therapy, which can selectively deliver to the mitochondria through a targeting unit, MitP. The cytotoxicity of PTPF-MitP to human lung tumor cells is twice as high as that of PTPF that does not have mitochondrial targeting units. In addition, it represents a real-time visualization and highly efficient treatment for tumor sites *in vivo*. This development represents a viable strategy for cancer therapy.

Keywords: porphyrin-based phototherapy, mitochondria targeting, real-time visualization, synergistic cancer therapy, hypoxia

INTRODUCTION

Phototherapy, typically as photodynamic therapy (PDT) and photothermal therapy (PTT), is achieved by photosensitizers (PSs) that absorb light energy to generate cytotoxic reactive oxygen species (ROS) or hyperthermia within near-infrared (NIR) laser irradiation, causing cell damage and even apoptosis [1,2]. Given that the local PSs are activated using specific wavelengths, phototherapy has the advantages of being non-invasive, highly selective, and repeatable without resistance to therapy [3]. Recently, several phototherapy schemes were prevailing for the treatment of various cancers, such as obstructive lung cancer [4], colon cancer [5], skin cancer [6,7], and bladder cancer [8].

However, the challenge is to enhance the efficacy of phototherapy [9–12], considering that the produced ROS exhibits a short half-life (<40 ns) and diffusion range (0.1 μm) in the phototherapy procedure [13–15]. It could be a great and promising choice for the comprehensive utilization of the generated cytotoxic substances (e.g., substantial ROS and hyperthermia) to antitumor. Mitochondria are among the essential organelles for cancer cells that play a central role in cell metabolism and the apoptotic pathway, where multiple forms of non-apoptotic cell death and necrosis-inducing biochemical cascades converge on the mitochondria [16–19]. Generally, mitochondria are susceptible to ROS and hyperthermia, which can cause mitochondrial dysfunction and even apoptosis. Recently [20], Jung *et al.* [21] reported that hyperthermia could enhance treatment by directing photothermal reagents to the mitochondria. Meanwhile, Noh *et al.* [22] developed a mitochondria-targeting photodynamic therapeutic reagent to enhance cancer treatment. Therefore, mitochondria-targeted O_2-evolving PDT and PTT synergistic strategies are promising strategies for solid tumor treatment since they can cause the complete death of cancer cells, improve therapeutic efficacy, and reduce the rate of unwanted side effects [23].

Herein, inspired by the strategy of "King Yu Tamed the Flood", where the flood was controlled by dredging the river, we designed a nanomissile integrated with O_2-evolving PDT and PTT, which could be accumulated in mitochondria in a targeted manner to unclog the pathway that releases cytochrome C and induces the apoptosis of tumor cells. Upon the 650-nm laser irradiation, excess ROS and hyperthermia caused mitochondrial dysfunction, releasing cytochrome C to activate the mitochondria-related apoptotic pathway and even induce the death of cancer cells [24,25].

The nanomissile was constructed by functionalizing porphyrin with folic acid (TCPP-PEG-FA), Pt nanoparticles (NPs) loaded-polydopamine (PDA@Pt), and fluorescein isothiocyanate-tagged lipocationic selective peptide (MitP-FITC; the structure is shown in Scheme S1). The designed PDA@Pt-TCPP-PEG-FA-MitP-FITC (PTPF-MitP) enhanced the cancer treatment efficiency by the following aspects: (i) hierarchical targeting strategy further improved the availability of nanomaterials. With the high affinity of folic acid to cell surface folic

[1] Key Laboratory of Bioelectrochemistry & Environmental Analysis of Gansu Province, College of Chemistry & Chemical Engineering, Northwest Normal University, Lanzhou 730070, China

[2] Tianjin Key Laboratory of Molecular Optoelectronic Science, Department of Chemistry School of Science, Tianjin University, Tianjin 300072, China

[3] Key Laboratory of Molecular Microbiology and Technology, Ministry of Education, Department of Microbiology, College of Life Science, Nankai University, Tianjin 300071, China

[†] These two authors contributed equally to this work.

[*] Corresponding authors (emails: luxq@nwnu.edu.cn (Lu X); zhzhen@tju.edu.cn (Zhang Z))

acid receptors, the folic acid derivatization facilitates the selective delivery of diagnostic and therapeutic agents to cancer cells through the cell membrane [26,27]. Moreover, MitP was used as a mitochondrial targeting unit. (ii) Pt NPs were loaded to overcome hypoxia by decomposing H_2O_2 to O_2, thus improving the O_2-dependent PDT effect. (iii) The tumor mitochondrial targeting delivery method initiated the irreversible apoptotic pathway during PDT and PTT. Therefore, a mitochondria-targeted nanotherapeutic system with the integrated excellent PDT and PTT would not only lead to a favorable suppression of the tumor but also provide guidance for the development of cancer therapeutic strategies.

EXPERIMENTAL SECTION

Materials and instruments

Meso-tetra(4-carboxyphenyl) porphyrin (TCPP) was synthesized in our laboratory (the synthetic method is shown in Supplementary Information). Polyethylene glycol (PEG) ($M_W = 4000$), *N*-hydroxysuccinimide (NHS), 3-hydroxytyramine hydrochloride (DA·HCl), and folic acid (FA) were obtained from 3AChemicals. Chloroplatinic acid hexahydrate ($H_2PtCl_6·6H_2O$), sodium borohydride ($NaBH_4$), and 1-(3-dimethylaminopropyl)-3-ethylcarbodiimide hydrochloride (EDC·HCl) were purchased from Aladdin. Ammonium hydroxide (30%) and fluorescein isothiocyanate-tagged lipocationic selective peptide (MitP-FITC) were obtained from Beijing Protein Innovation Ltd. All reagents were used without further purification. Deionized water used in our experiments was obtained from a Milli-Q water system. 1,ω-Diaminopolyoxyethylene ($M_W = 4000$) was synthesized according to the reported method with slight modification [28].

Ultraviolet-visible (UV-vis) absorbance measurements were performed on a Shimadzu UV-1750. Fourier transform infrared (FTIR) characterization was recorded on a Nicolet Nexus 670 FTIR spectrometer using KBr pellets. Transmission electron microscopy (TEM) images of the nanomaterials were obtained using a JEM-3010 TEM. High-resolution TEM (HRTEM) images were obtained on JEM-1400. Scanning electron microscopy (SEM) images were taken by using a field emission SEM (SU8010). Fluorescence spectroscopy was performed on an Edinburgh FS5 spectrophotometer. Powder X-ray diffraction (PXRD) analysis was conducted on RIGAKU SMARTLAB9KW (Japan) with Cu Kα ($\lambda = 1.5418$ Å). X-ray photoelectron spectrometer (XPS) was conducted using the VG ESCALAB MKII. Zeta potential and dynamic light scattering (DLS) of the samples were tested using Zetasizer Nano ZS90. Pt concentration was analyzed using Agilent 7700x inductively coupled plasma mass spectrometry (ICP-MS). ^1H nuclear magnetic resonance (^1H NMR) spectra were recorded on a Bruker Avance-400 (400 MHz) spectrometer at 25°C with dimethyl sulfoxide (DMSO-d$_6$) as the solvent and tetramethylsilane as the internal standard.

Synthesis of TCPP-PEG-FA

Synthesis of TCPP-PEG-FA (its structural formula is presented in Fig. S1): NH$_2$-PEG-FA was prepared according to the reported procedure with a slight change [29,30]. First, FA (44.1 mg, 0.1 mmol) was dissolved in DMSO (3 mL). Then, EDC·HCl (28.8 mg, 0.15 mmol) and NHS (17.3 mg, 0.15 mmol) were added to the above solution, followed by stirring for 12 h in darkness. Finally, NH$_2$-PEG-NH$_2$ (400 mg) was dissolved in

CHCl$_3$ (1 mL) and DMSO (2 mL), and functionalized FA was added to the above reaction solution, which was then stirred for 24 h. The product was precipitated in diethyl ether and dried in a vacuum.

TCPP-PEG-FA nanocomplexes were synthesized according to the published protocols with minor modifications [31]. First, TCPP (3.954 mg, 5 μmol) was mixed with EDC·HCl (1.917 mg, 10 μmol) and NHS (1.151 mg, 10 μmol) in DMSO (1 mL) for 30 min at 25°C in the dark. Then, the above-prepared NH$_2$-PEG-FA (40 mg) was slowly added to the above-activated TCPP molecules. After reacting for 24 h, excess TCPP molecules, catalysts, and DMSO were removed using Millipore filters (M_W = 8000–14,000) for 24 h. Afterward, the purified TCPP-PEG-FA was dissolved in deionized water (9 mL) and stored at −4°C for future use.

Synthesis of polydopamine (PDA) and PDA@Pt nanospheres

The PDA nanospheres with a size of 140 nm were synthesized *via* oxidation self-polymerization using the previous method [32]. Deionized water (45 mL), ethanol (20 mL), and ammonium hydroxide (1.5 mL) were stirred for 20 min at 30°C, and DA·HCl solution (250 mg, 25 mg mL^{-1}) was added directly to the reaction system, and stirred at 30°C for 24 h, resulting in a brownish-black-like solution. After purification by centrifugation at 10,000 r min^{-1}, the obtained PDA nanospheres were washed several times with deionized water. Finally, the product was dried at 50°C and collected for future use.

PDA@Pt nanospheres were prepared by mixing PDA powder (4 mg) with $H_2PtCl_6·6H_2O$ (6 mL, 4 mmol L^{-1}) solution under stirring for 1 h, followed by addition of NaBH$_4$ solution (600 μL, 4 mg mL^{-1}) and further stirring for 3 h. The product was purified by centrifuging at 10,000 r min^{-1} and washing several times with deionized water. At last, it was stored in deionized water (1 mL) at room temperature.

Synthesis of PTPF-MitP nanocomposite

The PTPF was synthesized by adding PDA@Pt (200 μL) and TCPP-PEG-FA (3 mL) to deionized water (10 mL). The reaction was allowed to proceed for 24 h at room temperature and in darkness, with constant stirring. After the reaction ended, the composite was collected *via* centrifugation at 10,000 r min^{-1}, washing with water several times and drying in a vacuum.

The PTPF-MitP nanocomposite was obtained by mixing PTPF (3 mg) dissolved in phosphate-buffered saline (PBS) (pH 7.4) with FITC-labeled MitP (100 μL, 5 mg mL^{-1}) under magnetic stirring for 12 h. After that, unconjugated FITC-labeled MitP were removed using Millipore filters (M_W = 8000–14,000). Finally, the purified PTPF-MitP were obtained and stored at −4°C for future use.

The PDA-TCPP-PEG-FA-MitP and PTPF were prepared under the same process except without Pt source and MitP unit.

Catalase activity detection of PTPF-MitP nanocomposite

The catalase activity of PTPF-MitP was recorded by measuring the absorbance of the remaining H_2O_2 concentration at 240 nm. The absorbance of the solution containing PTPF-MitP (30 μg mL^{-1}) and H_2O_2 (10 mmol L^{-1}) was recorded every 4 min while comparing with PDA-TCPP-PEG-FA-MitP dispersion (30 μg mL^{-1}) in the H_2O_2 (10 mmol L^{-1}). Meanwhile, the catalytic repeatability of PTPF-MitP was also operated by the addition of H_2O_2 (10 mmol L^{-1}) to the suspension every 30 min [33,34].

Singlet oxygen generation by PTPF-MitP nanocomposite

The 1,3-diphenylisobenzofuran (DPBF) was regarded as the trapping probe to determine the generation of singlet oxygen due to DPBF, which was easily oxidized by ROS, showing the obviously decreasing absorption at 410 nm. In the typical process, PTPF-MitP (2 μL, 3 mg mL^{-1}), PDA-TCPP-PEG-FA-MitP (2 μL, 3 mg mL^{-1}), H$_2$O$_2$ (10 μL, 10 mmol L^{-1}), DPBF (10 μL, 2.7 mg mL^{-1}, dissolved in acetonitrile), and 650 nm laser irradiation with a power density of 0.3 W cm^{-2} were used to measure the PDT efficiency. The UV-vis absorption of DPBF was recorded and compared in the presence or absence of H$_2$O$_2$, Pt NPs, and laser irradiation.

Mitochondrial recruitment assessment

The human lung tumor cells (A549) were treated with PTPF-MitP for 24 h at 37°C. After removing the culture medium, the incubated cells were washed with PBS several times, followed by staining with Hoechst 33342 (5 mg L^{-1}) for 1 h at 37°C and washing with PBS twice. Subsequently, the cells were stained with Mito-Tracker Red (100 nmol L^{-1}) for 30 min and observed through a confocal laser scanning microscope (CLSM).

Cytotoxicity assays

The CCK-8 Assay Kit (Dojindo) was utilized to evaluate the cell viability. A549 cells and mouse sarcoma (S180) cells were treated with PTPF and PTPF-MitP, respectively, at various concentrations ranging from 0 to 160 μg mL^{-1} for 24 h.

Cell viability assessment after irradiation

After the A549 cells and S180 cells were incubated with PTPF and PTPF-MitP (160 μg mL^{-1}) for 24 h, the treated cells were irradiated with 650 nm at a power density of 0.3 W cm^{-2} for 6 min. The CCK-8 Assay Kit was used to assess the cell viability after PDT and PTT. The cell death was recorded by means of propidium iodide (PI) staining [35].

Western blotting

The A549 cells were incubated with PTPF and PTPF-MitP, respectively, at the same concentration of 160 μg mL^{-1} for 24 h, and exposed to 650-nm irradiation for 6 min (cells with no irradiation were used for comparison), followed by the extraction of mitochondria. To detect both cytoplasmic and mitochondrial cytochrome C, the treated cells were homogenized with a Dounce homogenizer (20–50 strokes). The cell lysates were centrifuged at 1000 r min^{-1} and 4°C to remove nuclei and intact cells. The obtained suspension was then centrifuged at 10,000 r min^{-1} to get the supernatant cytoplasm and the pellet state of mitochondria, respectively. The levels of cytoplasmic and mitochondrial cytochrome C were detected with cytochrome C monoclonal antibody (Abcam) [36].

Animal model and fluorescence tracer *in vivo*

The female Balb/c mice (~20 g, Huafukang, China) were inoculated with S180 tumor cells (5×10^5 cells per mouse) near the lower limbs. After inoculation for seven days, PTPF-MitP (200 μL, 1 mg mL^{-1}) were intravenously injected into the mice, followed by the observation at 1, 2, and 24 h post-injection using the *in vivo* imaging system (Xenogen, IVIS Lumina II, USA).

Phototherapy *in vivo*

The female Balb/c mice with S180 tumors were intravenously injected with PTPF-MitP and PTPF (200 μL, 1 mg mL^{-1}), respectively, followed by irradiation with 650 nm laser (0.3 W cm^{-2}) for 6 min at 24 h. The tumor volume was calculated as (length) × (width)^2 × 1/2 with a caliper. The relative tumor volume was calculated as V/V_0, where V_0 and V indicated the tumor volume on the first day and the day of measurement. Tumor volumes were monitored for 12 more days. The mice were weighed, anesthetized, and sacrificed.

Ethical statement

All biological experiments, including the animal experiments and the cell culturing experiments, were conducted in accordance with the guidelines of the Animal Care and Use Committee of Nankai University and the experiment guidelines of the College of Life Science at Nankai University. The Committee approved all of the experiments.

Statistical analysis

Continuous data are presented as the mean ± standard deviation, while categorical data are presented as frequencies and percentages (%). Differences in the strains were compared using Student's *t*-test. All statistical analyses were performed using the SPSS Statistics Software (V20, IBM, USA).

RESULTS AND DISCUSSION

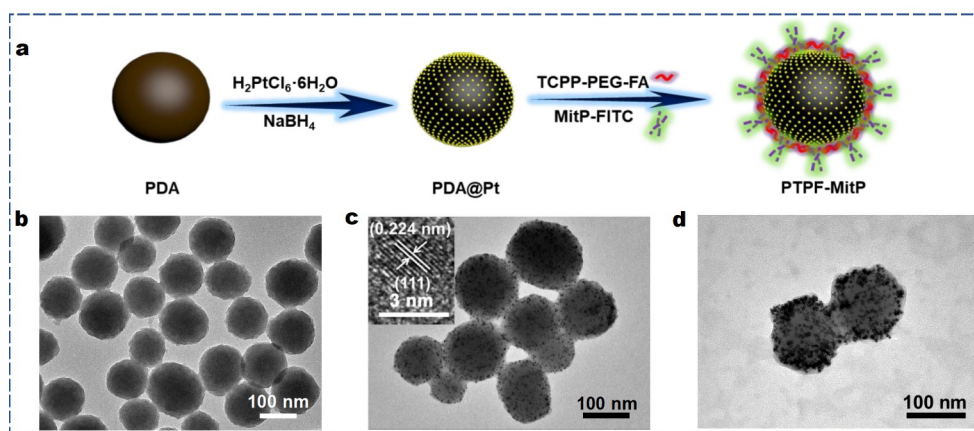The specific fabrication of nanocomposite is presented in Fig. 1a.

Figure 1 (a) Schematic illustration of the preparation procedure. (b) TEM images of PDA nanospheres, (c) PDA@Pt, and (d) PTPF-MitP nanocomposite. The inset in (c) is the HRTEM of Pt NPs.

First, PDA nanospheres were synthesized at 30°C *via* oxidation self-polymerization of dopamine under alkaline conditions (30% ammonia, pH 10). The uniform size and spherical morphology are displayed in TEM (Fig. 1b) and SEM images (Fig. S2a). The obtained PDA nanospheres had an average size of ~140 nm. Owing to the abundant amino and hydroxyl groups, PDA shows a weak reductive ability and often acts as coordination sites for metal ions [32]. Therefore, Pt^{4+} was reduced on the surface of PDA nanospheres by the addition of $NaBH_4$, and the morphology and size of the prepared PDA@Pt were similar to those of PDA nanospheres in TEM (Fig. 1c) and SEM images (Fig. S2b). The PXRD of PDA@Pt revealed the (111) and (200) crystal faces of cubic spinel Pt NPs (Fig. 2b) [37]. To further prove the size and structure of Pt NPs in the PDA@Pt, the HRTEM was operated (Fig. S3) and the obtained lattice spacing and size of Pt NPs were 0.224 and 3 nm (Fig. 1c).

Then, TCPP-PEG-FA was obtained *via* the amide reaction and further characterized by ^1H NMR, in which the appearance of the integral area of PEG polymers confirmed the presence of PEG polymers (Fig. S1). The synthesized TCPP-PEG-FA reacted with PDA@Pt to produce PTPF and then was further modified by MitP-FITC to form PTPF-MitP. As shown in the UV-vis spectra (Fig. 2a), the absorbance peaks of TCPP in PTPF-MitP were observed at 414, 515, 553, 583, and 636 nm, which were assigned to a major Soret band and four-Q bands [38]. These results present the successful graft of TCPP-PEG-FA. Moreover, the amount of TCPP onto the PTPF-MitP was also determined to be about 8.5 wt% according to the standard curve of free TCPP (Fig. S4). From the FTIR spectra (Fig. S5a), the specific peak was observed at 1098 cm^{-1} for the PTPF-MitP spectrum, which was assigned to $v_{as}(C–O–C)$ of PEG, indicating TCPP-PEG-FA was successfully grafted to PTPF-MitP. The peak at 1645 cm^{-1} was striking in the TCPP-PEG-FA spectrum, which was attributed to $v_{as}(C=O)$ in the amide bond. However, after the successful synthesis of PTPF-MitP, the absorbance at 1645 cm^{-1} disappeared, which was attributed to the coordination with Pt NPs.

To further demonstrate the successful synthesis of PTPF-MitP, as shown in the fluorescence spectroscopy of PTPF-MitP (Fig. S5b), the emission peaks of FA, FITC, and TCPP were observed at 346, 510, and 658 nm *via* the excitation of 270, 490, and 420 nm, respectively. Also, the size and morphology of the
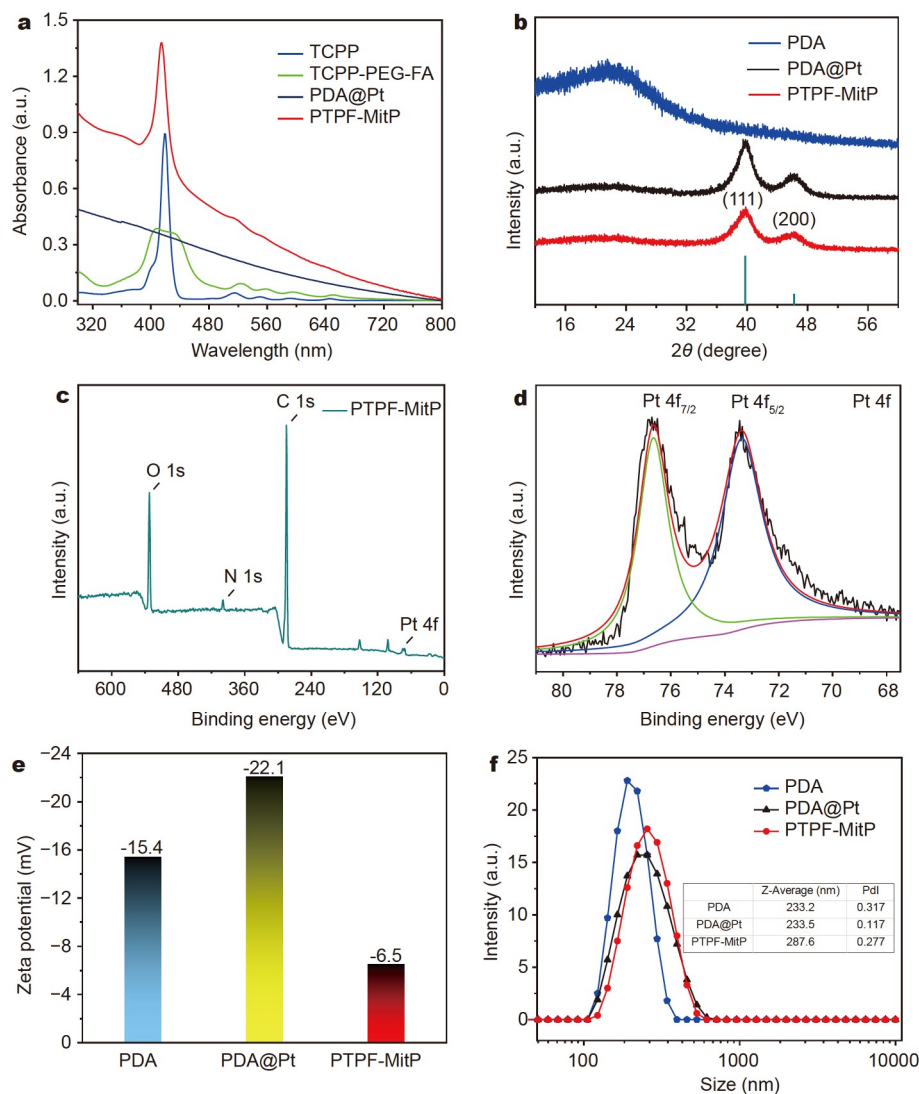

Figure 2 Spectra of TCPP, TCPP-PEG-FA, PDA@Pt, PTPF-MitP from the (a) UV-vis, (b) PXRD, (c, d) XPS, (e) zeta potential measurement, and (f) DLS.

resultant PTPF-MitP were exhibited by using TEM (Fig. 1d) and SEM images (Fig. S2c) having a size of 150 nm. In the PXRD patterns of PTPF-MitP (Fig. 2b), the peaks at 39.8° and 46.2° were assigned to (111) and (200) of the cubic spinel structure of Pt NPs (PDF#70-2057). Besides, Fig. 2c shows the XPS spectrum of PTPF-MitP, demonstrating the presence of Pt [39]. The peaks at 71.0 and 74.6 eV are attributed to Pt $4f_{7/2}$ and Pt $4f_{5/2}$, respectively (Fig. 2d). In addition, the ICP-MS showed that there was 6.8 wt% of Pt in PTPF-MitP. With the modification of PDA step by step, the change of zeta potentials was also displayed (Fig. 2e). Correspondingly, the hydrodynamic size increased to 287.6 nm by measuring DLS (Fig. 2f). Moreover, PTPF-MitP showed good solubility in various physiological solutions such as PBS, deionized water, and cell culture media, including 10% fetal bovine serum during a month (Fig. S6a). Meanwhile, the PTPF-MitP exhibited high biocompatibility demonstrated by the excellent dispersion stability in PBS for more than a week (Fig. S6b). After incubation with H_2O_2 (20 mmol L^{-1}) for 2 and 30 min, the characteristic absorption of the PTPF-MitP showed

neglectable changes, but the hydrodynamic size for the PTPF-MitP NPs increased from 287.6 to 338.1 nm (Fig. S7).

To certify that PTPF-MitP possessed an efficient catalase-like property, the time-dependent H_2O_2 decomposition was analyzed after the addition of PTPF-MitP, and as expected, enormous bubbles were observed in the tube after reacting for 20 min at room temperature. Meanwhile, the additional H_2O_2 was decomposed within 40 min by recording the specific absorbance of H_2O_2 at 240 nm (Fig. 3a). However, in the absence of Pt NPs, the H_2O_2 solution of PDA-TCPP-PEG-FA-MitP showed negligible bubbles under the same condition (Fig. 3b). It proved that PTPF-MitP retained highly sensitive recognition and catalysis toward H_2O_2, accompanying the burst of O_2. To simulate tumor conditions where H_2O_2 was continuously produced within tumor tissues [40,41], the catalytic activity of PTPF-MitP was further investigated by the repetitive addition of H_2O_2 three times, demonstrating that PTPF-MitP retained its persistent catalytic activity (Fig. 3c). Furthermore, the detailed concentration of the above additional H_2O_2 was also assessed according to
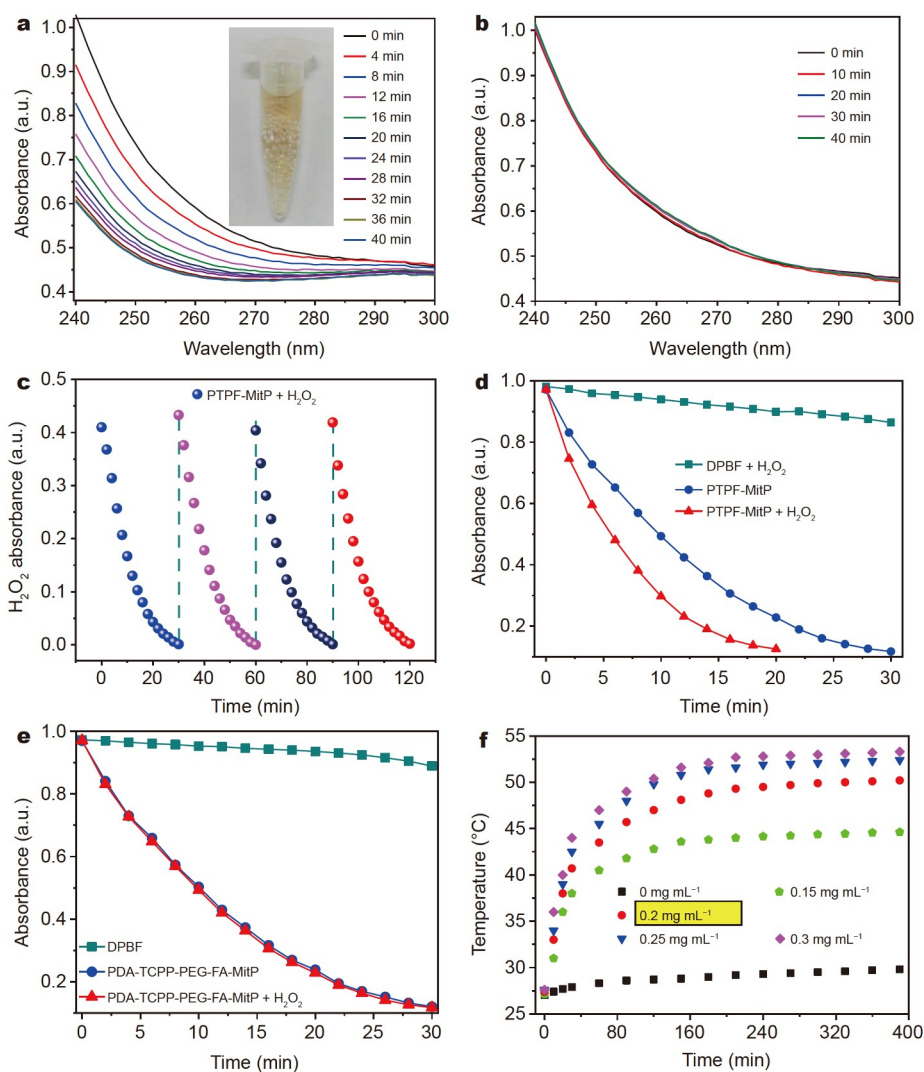

Figure 3 UV-vis spectra of the remaining H_2O_2 were recorded after reaction with (a) PTPF-MitP and (b) PDA-TCPP-PEG-FA-MitP in pH 7.4. The inserted photo in (a) indicates the production of countless gas bubbles. (c) Repeated decomposition by the addition of H_2O_2 to the PTPF-MitP solution. Attenuation curves of DPBF absorption at 410 nm in the (d) PTPF-MitP solution with or without H_2O_2 during different times of irradiation, (e) PDA-TCPP-PEG-FA-MitP solution with or without H_2O_2 during different times of irradiation. (f) Heating curves of PTPF-MitP at different concentrations under irradiation (650 nm, 0.3 W cm^{-2}).

the absorbance at 240 nm (Fig. S8a, b).

Since PTPF-MitP possessed catalytic capability toward H_2O_2, it could act as a nanofactory to produce O_2, enhancing the ROS generation of the O_2-dependent photodynamic process. As a significant component of ROS, singlet oxygen ($^1O_2$) played a crucial role in the death of cancer cells. Its generation capability was evaluated by using DPBF as a trapping probe (Fig. 3d, e and Fig. S9). A series of control experiments were operated under the same condition. First, the characteristic absorption peak of DPBF at 410 nm did not decrease obviously under laser irradiation in the presence or absence of H_2O_2, indicating that there are no $^1O_2$ molecules produced in the process (Fig. S9a₁, a₂). Then, there are similar results indicating that the presence of Pt was beneficial to the production of $^1O_2$ (Fig. S9b₁, c₁, c₂). As expected, the addition of H_2O_2 to the PTPF-MitP showed DPBF absorption at 410 nm apparently decreased within 20 min of irradiation (650-nm laser, 0.3 W cm^{-2}); however, the absence of H_2O_2 extended the time (Fig. 3d and Fig. S9b₁, c₁). Further experiments observed the key role of Pt NPs under the same

operation (Fig. 3d, e and Fig. S9c₁, c₂). The UV-vis absorption band of DPBF at 410 nm in the PTPF-MitP solution with H_2O_2 declined faster than PDA-TCPP-PEG-FA-MitP (without Pt) solution that contains H_2O_2 with light irradiation for up to 20 min (Fig. 3d, e). The higher $^1O_2$ level in the PTPF-MitP system demonstrated the outstanding ROS generation efficiency of the PTPF-MitP. Besides, the laser shows an almost equivalent influence on the generation ability of $^1O_2$. With the irradiation of the PDA-TCPP-PEG-FA-MitP solution, there was an obvious difference in the decrease of DPBF absorption at 410 nm (Fig. S9b₂, c₂). PDA-TCPP-PEG-FA-MitP could rapidly produce $^1O_2$ within 30 min, oxidating more DPBF compared with the absence of laser irradiation.

Having benefited from the broad absorption of PDA and TCPP in the NIR region (Fig. S10), the photothermal property of PTPF-MitP dispersed in PBS (pH 7.4) solution was verified as a function of concentration. PTPF-MitP solutions of 0.15, 0.20, 0.25, and 0.30 mg mL^{-1} were exposed to the 650-nm laser at a power density of 0.3 W cm^{-2} for different time periods, respec-
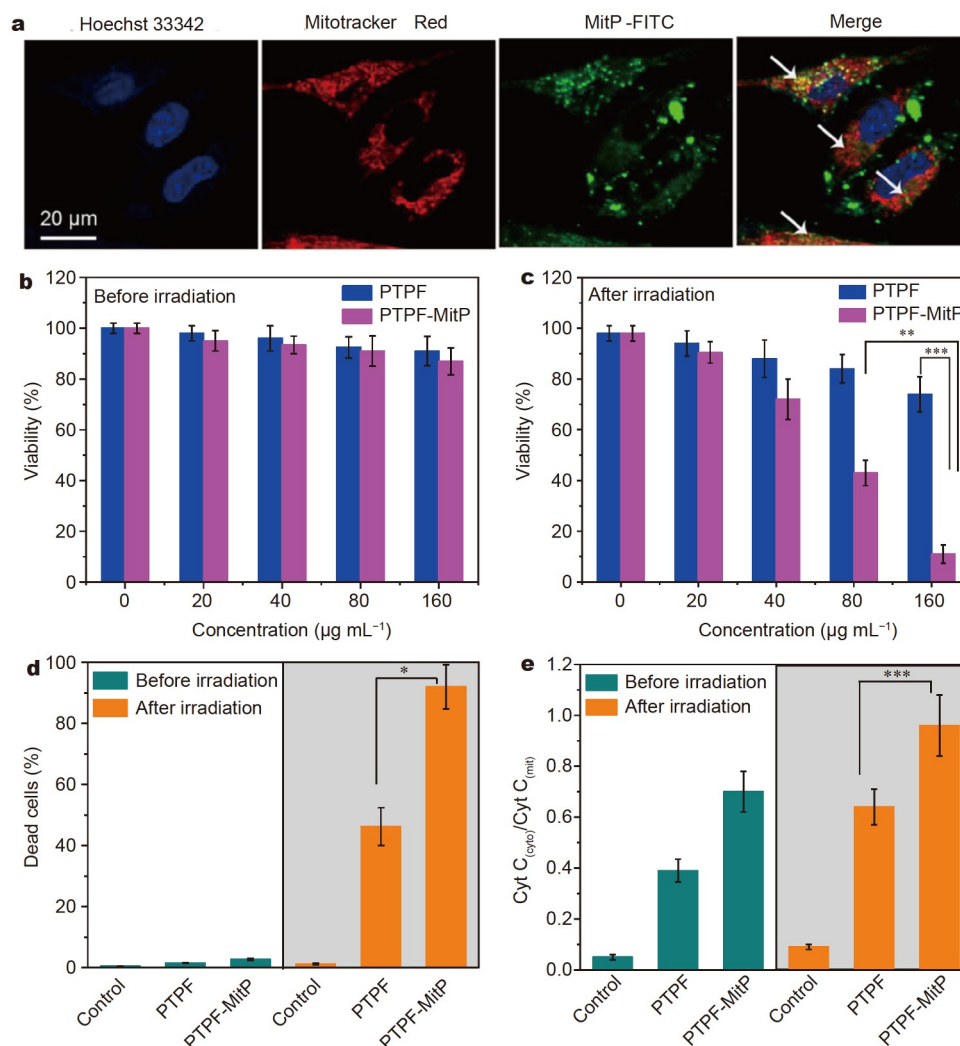

Figure 4 (a) CLSM images of the mitochondria-targeted illustration of PTPF-MitP in A549 cells after 4 h of co-incubation. Scale bars: 20 μm. (b, c) Viability of the cells treated with PTPF-MitP and PTPF at various concentrations in the dark and laser irradiation. (d) Dead cells stained with PI before and after irradiation. (e) Cytoplasmic and mitochondrial cytochrome C detected with cytochrome C monoclonal antibody (Abcam) with or without laser for PTPF-MitP and PTPF (650 nm, 0.3 W cm^{-2}). P-values were calculated by t-test (***$P < 0.001$, **$P < 0.01$, or *$P < 0.05$). Data were presented as mean ± standard deviation ($n = 5$).

tively. An obvious irradiation time- and concentration-dependent temperature increase was observed. After 6 min of irradiation, the temperature of the PTPF-MitP solution (0.2 mg mL^{-1}) quickly rose from 27.4 to 50.1°C (Fig. 3f). As the cancer cells can be effectively killed at temperatures of over 50°C for 4–6 min [32], the PTPF-MitP could be used as an ideal PTT reagent for the potential application in anticancer treatment.

It has been reported that the accumulation of ROS could induce and initiate the apoptotic pathway of cancer cells in the mitochondria [23,24]. It is expected the enhanced treatment effect on cancer cells can be observed by delivering nanodrugs to mitochondria. To confirm the assumption, first, the mitochondrial recruitment ability of PTPF-MitP was investigated by incubating A549 cells with PTPF-MitP for 24 h. The obtained nanomaterial-treated cancer cells were co-stained with organelle trackers, nuclei identified with Hoechst 33342, and mitochondria stained with Mito-Tracker Red. The CLSM revealed that the PTPF-MitP could gather mainly at the mitochondria in A549 tumor cells (indicated by white arrows) (Fig. 4a). Particularly, the cells treated with the PTPF-MitP exhibited dotted mitochondrial morphology, indicating a certain degree of mito-

chondrial damage. Subsequently, the cytotoxicity of PTPF-MitP and PTPF was evaluated before laser irradiation using the CCK-8 Assay Kit in A549 cells and S180 cells, showing the negative toxicity at concentrations of up to 160 μg mL^{-1} (Fig. 4b and Fig. S11a). In contrast, upon the laser irradiation, the cell viability of PTPF-MitP decreased dramatically to 11% at a concentration of 160 μg mL^{-1} compared with PTPF, which could be attributed to its MitP moiety, an excellent mitochondrial targeting unit; moreover, S180 cells showed lower cell viability of approximately 10% under the same condition (Fig. 4c and Fig. S11b). Simultaneously, the death percentage of PTPF-MitP or PTPF-loaded cells was also recorded as determined by PI-stained cells (Fig. 4d). After incubation with PTPF or PTPF-MitP NPs for 24 h, the mitochondria were destroyed to release cytochrome C from mitochondria. Particularly, in the PTPF-MitP system, much more cytochrome C was released for the mitochondrial targeting of MitP molecules. However, a short incubation period (24 h) provided a relatively weak response, making both PTPF and PTPF-MitP NPs not show obvious cell-killing effects before laser irradiation, which is consistent with a previous report [34]. Consequently, PTPF-MitP showed excellent cytotoxicity when
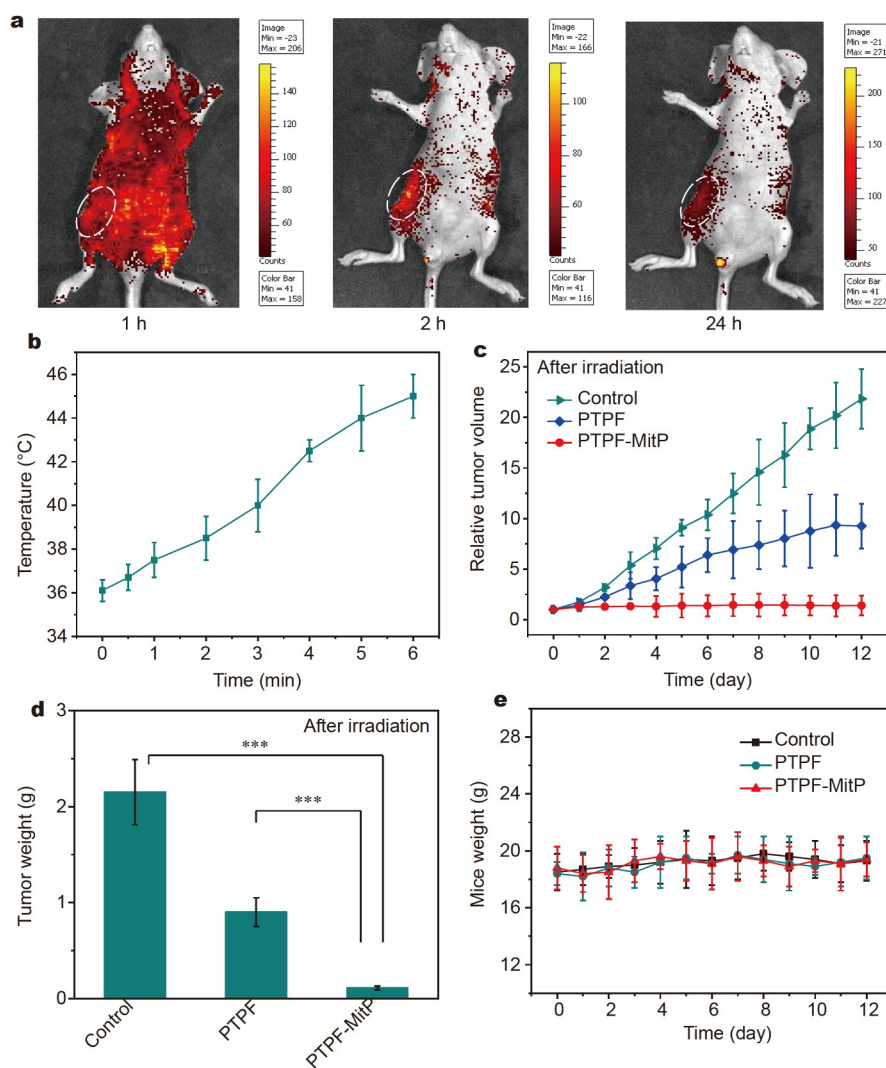

Figure 5 (a) Biodistribution of PTPF-MitP in mice bearing S180 tumor cells. (b) The temperature curve of tumors treated with PTPF-MitP and laser irradiation. (c) Relative tumor volume curves. (d) Weights of excised tumors. (e) Bodyweight variations of mice. The *P*-values were calculated using Student's *t*-test (***P< 0.001). Continuous data are presented as mean ± standard deviation (*n* = 3).

the cells were irradiated and localized by a mitochondrial targeting unit, up to twice as much as PTPF. The enhanced cytotoxicity of PTPF-MitP might depend on mitochondrial dysfunction because of hyperthermia and excess ROS in the mitochondria, inducing and triggering the death of cancer cells (Scheme S2). It was reported that the release of cytochrome C could act as a significant apoptotic signal [42,43]. Therefore, changes in cytochrome C in the mitochondria were recorded using cytochrome C monoclonal antibody (Fig. 4e). The results showed that the production of ROS in the PTPF could damage the mitochondria to a certain extent but the targeted recruitment of PTPF-MitP to the mitochondria caused severer and irreversible destruction, up to 1.6 times that of PTPF, after the irradiation.

On the basis of the above *in vitro* results, PTPF-MitP was also promising for PDT and PTT with its synergistically suppressive effects on tumor growth. The PTPF-MitP (200 μL, 1 mg mL^{-1}) was intravenously injected into the mice bearing the solid tumors *via* the red fluorescence of TCPP to trace the distribution of PTPF-MitP *in vivo* (Fig. 5a). Compared with injection time at 1 and 24 h, a significant fluorescence of PTPF-MitP was observed in tumor tissues after injecting at 2 h. For mice injected with PTPF-MitP, the tumor temperature rapidly increased to 45°C after being irradiated for 6 min (Fig. 5b), which was suitable for low-temperature PTT. Next, the therapeutic effect of PDT and PTT using PTPF-MitP was evaluated by monitoring the tumor volume after local laser irradiation (Fig. 5c). Compared with the control experiment, no obvious suppression effect was observed for PTPF. Notably, the tumor was dramatically suppressed for PTPF-MitP with irradiation. Tumor weight was also recorded, showing an obvious decrease in PTPF-MitP (Fig. 5d). Also, there were no significant body weight changes in each group during the treatment, which proved that all treatments had negligible side effects (Fig. 5e).

CONCLUSIONS

In summary, a novel mitochondria-targeted phototherapy nanomaterial, PTPF-MitP, was fabricated with three functional groups: (i) MitP as the mitochondrial targeting unit, (ii) TCPP as the NIR fluorescent signaling unit, and (iii) PDA and TCPP as the excellent PTT and PDT reagent, respectively. In addition, Pt NPs act as a nanozyme to decompose H_2O_2 to O_2, relieving the hypoxic microenvironment of tumor cells. In A549 cells, PTPF-MitP was localized to the mitochondria, showing its excellent phototherapy effect. Furthermore, by the selective delivery of PTPF-MitP to the mitochondria and the achievement of PDT/PTT-combined hypoxic cancer treatment under NIR laser irradiation, the tumors were obviously suppressed *in vivo*. The designed novel nanotherapeutic system not only remarkably improves the PDT and PTT therapeutic effects for solid tumors under hypoxic environments by targeting mitochondria but also broadens the horizon for cancer therapy by targeting PDT and PTT in the mitochondria.

1   Lucky SS, Soo KC, Zhang Y. Nanoparticles in photodynamic therapy. Chem Rev, 2015, 115: 1990–2042
2   Dolmans DEJGJ, Fukumura D, Jain RK. Photodynamic therapy for cancer. Nat Rev Cancer, 2003, 3: 380–387
3   Lin H, Yang L, Zhang X, *et al.* Emerging low-dimensional nanoagents for bio-microimaging. Adv Funct Mater, 2020, 30: 2003147
4   Allison R, Moghissi K, Downie G, *et al.* Photodynamic therapy (PDT) for lung cancer. Photodiagnosis Photodynamic Ther, 2011, 8: 231–239
5   Lu K, He C, Lin W. A chlorin-based nanoscale metal-organic framework for photodynamic therapy of colon cancers. J Am Chem Soc, 2015, 137: 7600–7603
6   Brown SB, Brown EA, Walker I. The present and future role of photodynamic therapy in cancer treatment. Lancet Oncology, 2004, 5: 497–508
7   Kostovic K, Pastar Z, Ceovic R, *et al.* Photodynamic therapy in dermatology: Current treatments and implications. Coll Antropol, 2012, 36: 1477–1481
8   Yavari N, Andersson-Engels S, Segersten U, Malmstrom PU. An overview on preclinical and clinical experiences with photodynamic therapy for bladder cancer. Can J Urol, 2011, 18: 5778–5786
9   Liu Y, Wu S, Liu Y, *et al.* Cathodic protected Mn^{2+} by Na_xWO_3 nanorods for stable magnetic resonance imaging-guided tumor photothermal therapy. Biomaterials, 2020, 234: 119762
10 Kim J, Cho HR, Jeon H, *et al.* Continuous O_2-evolving $MnFe_2O_4$ nanoparticle-anchored mesoporous silica nanoparticles for efficient photodynamic therapy in hypoxic cancer. J Am Chem Soc, 2017, 139: 10992–10995
11 Zheng DW, Li B, Li CX, *et al.* Carbon-dot-decorated carbon nitride nanoparticles for enhanced photodynamic therapy against hypoxic tumor *via* water splitting. ACS Nano, 2016, 10: 8715–8722
12 Tang Z, Zhang H, Liu Y, *et al.* Antiferromagnetic pyrite as the tumor microenvironment-mediated nanoplatform for self-enhanced tumor imaging and therapy. Adv Mater, 2017, 29: 1701683
13 Huang P, Lin J, Wang X, *et al.* Light-triggered theranostics based on photosensitizer-conjugated carbon dots for simultaneous enhanced-fluorescence imaging and photodynamic therapy. Adv Mater, 2012, 24: 5104–5110
14 Pan M, Jiang Q, Sun J, *et al.* Programming DNA nanoassembly for enhanced photodynamic therapy. Angew Chem Int Ed, 2020, 59: 1897–1905
15 Liu Y, Zhai S, Jiang X, *et al.* Intracellular mutual promotion of redox homeostasis regulation and iron metabolism disruption for enduring chemodynamic therapy. Adv Funct Mater, 2021, 31: 2010390
16 Kroemer G, Reed JC. Mitochondrial control of cell death. Nat Med, 2000, 6: 513–519
17 Weinberg SE, Chandel NS. Targeting mitochondria metabolism for cancer therapy. Nat Chem Biol, 2015, 11: 9–15
18 Wallace DC. Mitochondria and cancer. Nat Rev Cancer, 2012, 12: 685–698
19 Xiao T, Fan JK, Huang HL, *et al.* VEGI-armed oncolytic adenovirus inhibits tumor neovascularization and directly induces mitochondria-mediated cancer cell apoptosis. Cell Res, 2010, 20: 367–378
20 Rangasamy S, Ju H, Um S, *et al.* Mitochondria and DNA targeting of 5,10,15,20-tetrakis(7-sulfonatobenzo[*b*]thiophene) porphyrin-induced photodynamic therapy *via* intrinsic and extrinsic apoptotic cell death. J Med Chem, 2015, 58: 6864–6874
21 Jung HS, Han J, Lee JH, *et al.* Enhanced NIR radiation-triggered hyperthermia by mitochondrial targeting. J Am Chem Soc, 2015, 137: 3017–3023
22 Noh I, Lee DY, Kim H, *et al.* Enhanced photodynamic cancer treatment by mitochondria-targeting and brominated near-infrared fluorophores. Adv Sci, 2018, 5: 1700481
23 Shah BP, Pasquale N, De G, *et al.* Core-shell nanoparticle-based peptide therapeutics and combined hyperthermia for enhanced cancer cell apoptosis. ACS Nano, 2014, 8: 9379–9387
24 Liu X, Kim CN, Yang J, *et al.* Induction of apoptotic program in cell-free extracts: Requirement for dATP and cytochrome c. Cell, 1996, 86: 147–157
25 Cai J, Yang J, Jones DP. Mitochondrial control of apoptosis: The role of cytochrome c. Biochim Biophysica Acta-Bioenergetics, 1998, 1366: 139–149
26 Wang S, Low PS. Folate-mediated targeting of antineoplastic drugs, imaging agents, and nucleic acids to cancer cells. J Control Release,

1998, 53: 39–48

27 Zhang Z, Jia J, Lai Y, et al. Conjugating folic acid to gold nanoparticles through glutathione for targeting and detecting cancer cells. Bioorg Medicinal Chem, 2010, 18: 5528–5534

28 Wang B, Hai J, Liu Z, et al. Selective detection of iron(III) by rhodamine-modified Fe_3O_4 nanoparticles. Angew Chem Int Ed, 2010, 49: 4576–4579

29 Wang B, Hai J, Wang Q, et al. Coupling of luminescent terbium complexes to Fe_3O_4 nanoparticles for imaging applications. Angew Chem Int Ed, 2011, 50: 3063–3066

30 Peng Y, Wang Z, Liu W, et al. Size- and shape-dependent peroxidase-like catalytic activity of $MnFe_2O_4$ nanoparticles and their applications in highly efficient colorimetric detection of target cancer cells. Dalton Trans, 2015, 44: 12871–12877

31 Cheng L, Jiang D, Kamkaew A, et al. Renal-clearable PEGylated porphyrin nanoparticles for image-guided photodynamic cancer therapy. Adv Funct Mater, 2017, 27: 1702928

32 Liu Y, Ai K, Liu J, et al. Dopamine-melanin colloidal nanospheres: An efficient near-infrared photothermal therapeutic agent for in vivo cancer therapy. Adv Mater, 2013, 25: 1353–1359

33 Zhang Y, Wang F, Liu C, et al. Nanozyme decorated metal-organic frameworks for enhanced photodynamic therapy. ACS Nano, 2018, 12: 651–661

34 Ye J, Li Z, Fu Q, et al. Quantitative photoacoustic diagnosis and precise treatment of inflammation in vivo using activatable theranostic nanoprobe. Adv Funct Mater, 2020, 30: 2001771

35 Yu Q, Zhang B, Li J, et al. The design of peptide-grafted graphene oxide targeting the actin cytoskeleton for efficient cancer therapy. Chem Commun, 2017, 53: 11433–11436

36 Yu Q, Zhang YM, Liu YH, et al. Magnetism and photo dual-controlled supramolecular assembly for suppression of tumor invasion and metastasis. Sci Adv, 2018, 4: eaat2297

37 Song Y, Shi Q, Zhu C, et al. Mitochondrial-targeted multifunctional mesoporous Au@Pt nanoparticles for dual-mode photodynamic and photothermal therapy of cancers. Nanoscale, 2017, 9: 15813–15824

38 Pu G, Zhang D, Mao X, et al. Biomimetic interfacial electron-induced electrochemiluminesence. Anal Chem, 2018, 90: 5272–5279

39 Wang XS, Zeng JY, Zhang MK, et al. A versatile Pt-based core-shell nanoplatform as a nanofactory for enhanced tumor therapy. Adv Funct Mater, 2018, 28: 1801783

40 Halliwell B, Clement MV, Long LH. Hydrogen peroxide in the human body. FEBS Lett, 2000, 486: 10–13

41 Li Q, Ge X, Ye J, et al. Dual ratiometric SERS and photoacoustic core-satellite nanoprobe for quantitatively visualizing hydrogen peroxide in inflammation and cancer. Angew Chem Int Ed, 2021, 60: 7323–7332

42 Zhivotovsky B, Orrenius S, Brustugun OT, et al. Injected cytochrome c induces apoptosis. Nature, 1998, 391: 449–450

43 Liu Y, Zhang J, Zuo C, et al. Upconversion nano-photosensitizer targeting into mitochondria for cancer apoptosis induction and cyt c fluorescence monitoring. Nano Res, 2016, 9: 3257–3266

Author contributions Lu X and Zhang Z designed the study and supervised the project; Shang D conceived the experimental scheme and performed the experiments; Yu Q carried out the in vitro and in vivo experiments; Liu W, Zhang S, Li Y, and Chen J performed data analysis; Shang D wrote the paper with support from Zhang Z. All authors contributed to the general discussion.

Conflict of interest The authors declare that they have no conflict of interest.

Supplementary information Supporting data are available in the online version of the paper.

Denghui Shang received her BSc and MSc degrees from the College of Chemistry and Chemical Engineering, Northwest Normal University. She is currently pursuing her PhD degree at Tianjin University under the supervision of Prof. Li. Her research focuses on the design of catalysts for wastewater treatment.

Zhen Zhang obtained his PhD degree from the Institute of Chemistry, Chinese Academy of Sciences in 2017, after which he joined Tianjin University as a lecturer in 2017. He was a visiting scholar in the laboratory of Prof. Yadong Yin at the University of California (Riverside) in 2019–2020. His scientific interest is mainly focused on the design and fabrication of functional nanomaterials and related applications.

Xiaoquan Lu received his BSc and MSc degrees from the Department of Chemistry, Northwest Normal University in 1994, and his PhD degree from Sun Yat-sen University in 1997. He was a visiting scholar at Changchun Institute of Applied Chemistry, Chinese Academy of Sciences in 2001. His research interests are bioelectrochemistry, visual sensing, and new energy development.

基于卟啉的荧光成像介导线粒体靶向光动力/光热协同癌症治疗

尚登辉[1,2†], 喻其林[3†], 刘伟[2], 张守婷[2], 李轶[2], 陈晶[1], 张振[2*], 卢小泉[1*]

摘要 线粒体是细胞的动力中心, 在激活癌细胞凋亡通路中起关键作用. 而线粒体易受具有细胞毒性的活性氧物种(ROS)和局部过热的影响. 本文中, 我们开发了一种线粒体靶向的"纳米导弹", 即卟啉接枝的聚多巴胺纳米材料(PTPF-MitP), 它具有自供氧的光动力治疗(PDT)和光热治疗(PTT)的特性, 通过靶向单元MitP选择性地传递至线粒体, 在650 nm激光刺激下, 线粒体功能遭到严重的损伤, 释放凋亡因子细胞色素C (Cyt C), 从而激活癌细胞的凋亡途径, 增强肿瘤的治疗效果. 体外实验发现此纳米药物对人肺肿瘤细胞(A549)的细胞毒性比缺乏线粒体靶向单元的PTPF提高了2倍, 此外, 它对小鼠体内的肿瘤表现出实时可视化和高效抑制作用. 这为癌症治疗策略的发展提供了有力指导.